Coupling of perinuclear actin cap and nuclear mechanics regulates flow-induced YAP spatiotemporal nucleocytoplasmic transport

Tianxiang Ma#[1], Xiao Liu#*[,1], Haoran Su#[1], Shangyu Li[3,4], Chenxing Gao[1], Zhuqing Liang[1], Dongrui Zhang[1], Xing Zhang[1], Kexin Li[1], Ke Hu[1], Li Wang[1], Min Wang[5], Fan Wu[1], Shuhua Yue[1], Weili Hong[1], Xun Chen[1], Xiaoyan Deng[1], Pu Wang*[,1] and Yubo Fan*[,1,2]

1 Beijing Advanced Innovation Centre for Biomedical Engineering, Key Laboratory for Biomechanics and Mechanobiology of Chinese Education Ministry, School of Biological Science and Medical Engineering, Beihang University, Beijing 100083, China

2 School of Engineering Medicine, Beihang University, Beijing 100083, China

3 Biomedical Pioneering Innovation Center (BIOPIC), Peking University, Beijing 100871, China

4 Academy for Advanced Interdisciplinary Studies, Peking University, Beijing 100871, China

5 Department of Gynecology and Obstetrics , Strategic Support Force Medical Center ,Beijing 100101,China

#These authors contributed equally to this work.

*Address for correspondence: Dr. Liu, Dr. Wang and Dr. Fan, School of Biological Science & Medical Engineering, Beihang University, Beijing 100191, China. Tel.: +86 10 8233 9724; Fax: +86 10 8233 9962; E-mail: liuxiao@buaa.edu.cn, puwang@buaa.edu.cn, yubofan@buaa.edu.cn

Summary

Flow shear stress controls fundamental behaviors of cells. It can modulate nuclear mechanotransduction through regulating the transport of transcriptional activators such as Yes-associated protein (YAP) from cytoplasm to nucleus. However, the mechanism how flow induces the nucleocytoplasmic transport remains largely unclear. Here we show that flow applied to endothelial cells not only drives polarized actin reorganization but also alters nuclear mechanics, which synergically controls nuclear deformation, resulting in YAP nucleocytoplasmic transport through combination of biological experiments and mechanochemical models. We discovered that unidirectional flow induces simultaneous actin caps formation and nuclear stiffening in a dose and timing-dependent manner, which causes YAP initially entering the nucleus, but then gradually exporting. Additionally, pathological oscillatory flow affects the mechanotransduction by forming slight actin cap and softening nucleus, which sustains YAP nuclear localization. Our work unveils a mechanism of flow-induced nucleocytoplasmic transport, which potentially provides a universal linkage between transcriptional regulation and mechanical stimulation.

Keywords: Wall shear stress, YAP, actin cap, nucleus, mechanotransduction, mechanochemical model

Introduction

Human cells are constantly subjected to distinct mechanical cues, such as extracellular matrix viscoelasticity[1], stretched or compressive forces[2], and flow shear stress[3]. Sensing and correctly responding to these biomechanical stimulations are fundamental aspects of cellular functions. For instance, shear stress, the friction force induced by blood flow, lymphatic and interstitial flow, is known to actively participate in endothelial and tumor cells proliferation, apoptosis, invasion, and metastasis[4-6]. Therefore, it plays a major role in diseases such as atherosclerosis and cancer[7-11].

Yes-associated Protein (YAP) is emerging as a universal mechanotransducer and mechanoeffector which is capable of responding to a variety of biomechanical signals such as flow shear stress[12-14]. The main regulatory mechanism of YAP is dependent on its transport from cytoplasm to nucleus, where it acts as a transcriptional coactivator, binds to and activates TEAD transcription factors[15]. One well-studied biochemical mechanism is that YAP acts as a downstream effector of the Hippo signaling pathway, whose activation inhibits YAP by inducing YAP phosphorylation and cytoplasmic retention[14]. In addition, flow-induced regulation of F-actin polymerization has shown to be associated with nuclear localization of YAP which is released from angiomotin (AMOT)[12,13,16]. However, confounding results with both cytoplasmic retention and nuclear localization of YAP have been found when endothelial cells (ECs) exposed to laminar flow while F-actin polymerization, suggesting that the YAP nucleocytoplasmic shuttling may be also regulated by other mechanisms[17-19].

Recent studies revealed that mechanical forces delivered to the nucleus can deform the nuclear membrane to control the permeability of nuclear pores[20,21]. It suggests that mechanical rather than biochemical cues regulate YAP nucleocytoplasmic shuttling as they found out flow shear stress deforms the nucleus through the cytoskeleton. On the other hand, more studies have shown that perinuclear actin cap is a highly organized subset of tensed actin filaments that are tightly linked to the nucleus and exert higher tension than conventional actin fibers[22,23]. In addition, the alteration of nuclear stiffness induced by factors such as chromatin condensation also affects nuclear membrane deformation[24]. Based on these clues, we hypothesize that the YAP nucleocytoplasmic shuttling under different flow conditions is regulated by the nuclear deformability, which is controlled by interactions among shear stress transduction, actin fiber organization, and nuclear mechanics. To verify the hypothesis, we combined microfluidic vascular chip, Brillouin microscopy and theoretical mechano-chemical three-dimensional model to unveil the spatiotemporal nucleocytoplasmic transport of vascular endothelial cells under both unidirectional laminar flow and oscillatory flow. We show that unidirectional laminar flow causes the actin cap to form directly above the nucleus, which is accompanied by nuclear chromatin condensation as stiffness increases. YAP would initially enter the nucleus rapidly, but it is then gradually exported from the nucleus, generating low YAP intensity ratio of nucleus to cytoplasm. With the proposed theoretical model, we found that the spatiotemporal nucleocytoplasmic transport of YAP is synergistically determined by formation of actin cap and nuclear

stiffening, corelates with the deformation of nuclear membrane. We then expand our framework to explore how oscillatory flow affects the mechanotransduction and sustains YAP localization in nucleus. The result coincides with that in unidirectional flow study, which the coupling of actin cap and nuclear mechanics synergistically determines the YAP transport.

Results

Unidirectional laminar shear stress induces simultaneous formation of actin caps and nuclear stiffening in a dose and timing-dependent manner.

As actin filament and nucleus of vascular endothelial cells (ECs) adapts to the direction of blood flow[25,26], we first investigated the morphological mechanoresponse of ECs to unidirectional laminar shear stress (LS) using a microfluidic system with adjustable magnitude and timing of applied flow. Confocal microscopy was used to examine actin and nuclear three-dimensional organization, which were stained with phalloidin and 4',6-diamidino-2-phenylindole (DAPI), respectively. We noted that ECs subjected to LS (12 dyne/cm^2, 24 hours) would form organized basal conventional fibers and apical actin cap to the nucleus of cells, which were accompanied by an increase in nuclear chromatin compaction (Figure 1A). The quantification of actin filament of ECs in response to different shear stress magnitudes and shearing times revealed a gradual, time-dependent polarization of conventional fibers and actin cap formation (Figure 1B-1C, Figure S1A). When compared to static control, LS of both 12 dyne/cm^2 and 4 dyne/cm^2 would promote conventional fibers polarization, which is more pronounced after 15 hours for 12 dyne/cm^2 and 48 hours for 4 dyne/cm^2 of shear stress and only slowly increases until then (Figure 1B). Intriguingly, while LS at 12 dyne/cm^2 for 15 hours did not cause conventional fibers polarization, this regime did trigger actin cap formation (Figure 1C). Similarly, 24 hours of LS at 4 dyne/cm^2 can cause actin cap formation but not conventional fibers polarization, implying that the actin cap is more sensitive to laminar flow than conventional fibers reorganization.

We next investigated how shear stress affected the nuclear stiffness in a non-destructive, label- and contact-free manner through Brillouin microscopy (Figure 1D). To ensure that our custom-made Brillouin microscopy can reliably assess the stiffness in biological samples, we explored the information content of Brillouin spectrum of gelatin methacryloyl (GelMA) hydrogels and compared it to uniaxial compression test. We found both the Brillouin shift measured by Brillouin microscopy and Young's modulus measured by uniaxial compression tests are positively correlated with the GelMA concentrations (Figure S1B), whose mechanical moduli covers most lives cells and organisms[27]. We found that the nucleus stiffness under shear stress increased with increasing shear time for both 12 dyne/cm^2 and 4 dyne/cm^2, with the mean Brillouin shift gradually increasing from 7.675±0.008 GHz to 7.824±0.012 GHz ($P<0.0001$) and 7.736±0.017 GHz ($P<0.0001$), respectively (Figure 1E-1F). Since the nucleus stiffness is highly correlated with chromatin compaction[28,29], we further assessed the flow-induced alteration of DNA signal heterogeneity across the nucleus through a metric of the coefficient of variation (CV),

which is defined as the ratio of the standard deviation of DAPI intensity to the mean[30]. As expected, changes in CV are in parallel with the trend in Brillouin shift measured by Brillouin microscopy, and positively correlated with shear time (Figure 1G).

Collectively, these data indicate that the actin cap formation as well as the nuclear stiffening are synchronized under LS, affected by its magnitude and timing.

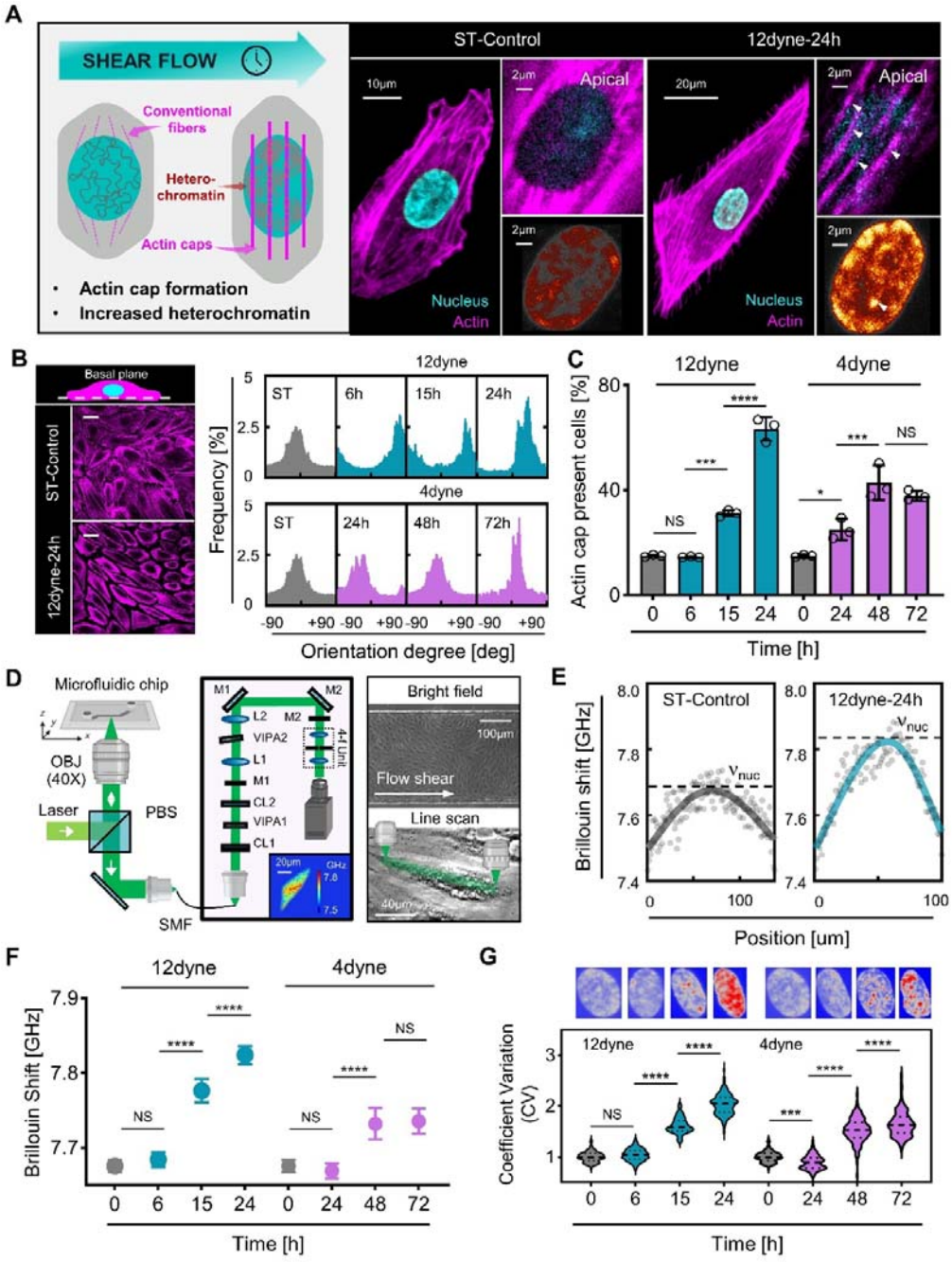

Figure 1. The simultaneous formation of actin cap and nuclear stiffening under shear stress.

(A) Schematic of cell subjected to laminar shear stress (LS) with increasing actin cap formation and heterochromatin. Representative cells (stained by DAPI and phalloidin

for nucleus and actin filament), chromatin compaction (stained by DAPI with the smart LUT applied), and actin caps (apical views) under static control (ST) and LS of 12 dyne/cm^2 for 24 hours. Arrowhead indicates the actin cap and heterochromatin region under LS.

(B) Representative basal conventional fibers organization (stained by phalloidin) under ST control and LS of 12 dyne/cm^2 for 24 hours. Quantification of F-actin shows time-dependent polarization of conventional fibers in response to LS under both 4 dyne/cm^2 and 12 dyne/cm^2 (frequency distribution of >100 cells/condition pooled across three independent experiments). Scale bars, 40μm.

(C) Flow-dependent formation of actin cap under LS of 12 dyne/cm^2 and 4 dyne/cm^2 (n=3 independent experiments with > 100 cells/condition, NS: p> 0.05, *p < 0.05, ***p < 0.001, ****p < 0.0001. Error bars represent ±SD).

(D) Setup of label-/contact-free Brillouin microscopy combined with the microfluidic vascular chip. The representative bright field image of cells cultured in the microfluidic channel, and the schematic of line scan Brillouin measurements across the long axis of cells.

(E) Representative Brillouin shift from the line scan across the cell under ST, LS of 12 dyne/cm^2 for 24 hours, and LS of 4 dyne/cm^2 for 72 hours. The scattering data was fitted by smoothing spline, and the dash line indicates the maximum Brillouin shift of the nucleus.

(F) A time-dependent increase in Brillouin shift is observed between nucleus under ST and LS of 12 dyne/cm^2 and 4 dyne/cm^2 (n=5 for each condition, NS: p> 0.05, *p < 0.05, ****p < 0.0001. Error bars represent ±SD).

(G) Representative images of chromatin compaction (stained by DAPI with the phase LUT applied) under ST and LS. Quantification of time-dependent increase in coefficient of variation (CV) of the nucleus between groups under ST and LS (n=3 independent experiments with > 100 cells/condition, NS: p> 0.05, ***p < 0.001, ****p < 0.0001).

The interplay of actin cap and nuclear mechanics regulates the flow-induced YAP nucleocytoplasmic transport.

YAP has been utilized as a paradigm of mechanosensitive transcription factors to investigate the nucleoplasmic transport patterns[20,21]. Our primary metric for YAP translocation, as in previous studies, is the ratio of YAP fluorescence intensity in the nucleus to that in the cytoplasm, hence the term YAP ratio (YR). To investigate how cellular interactions with the shear stress influence YAP localization, we firstly measured the YR in cells exposed to shear stress with magnitude of 12 dyne/cm^2 and 4 dyne/cm^2. Cells exposed to both shear stress magnitudes showed a tendency for YAP to initially enter the nucleus, but then gradually export from the nuclear, *i.e.*, YR increases and then decreases (Figure 2A-2B). At shear stress of 12dyne/cm^2, YAP transport influxes the nucleus at 0-6 hours and effluxes at 6-24 hours, while at 4dyne/cm^2, the entrance of YAP would prolong to 24 hours and the exist of the nucleus could slowly last to 72 hours, which implies that high flow shear speeds up the YR transfer rate.

We next investigated whether actin cap and nuclear stiffness regulates the nucleocytoplasmic shuttle of YAP under flow. We first treated ECs with actin polymerization inhibitor latrunculin B (LatB) of different dose to affect the actin reorganization while maintain the integral function of ECs (Figure S2A). To suppress only the actin cap without affecting the conventional actin fibers, we treated cells with low doses of LatB (<60nM) for short periods (<1 hour)[31] (Figure 2C). Treatment with 30nM and 60nM LatB differentially inhibit the actin cap formation in ECs subjected to shear, leading to cells with the actin cap decreasing from 63.34±4.49% of the control to 38.18±1.59% ($P < 0.01$) and 4.25±2.38% ($P < 0.001$), respectively (Figure 2D). In addition, the LatB treatment also reduces flow-induced chromatin condensation and nuclear stiffness (Figure 2E-2F). When both actin cap and nuclear stiffening are inhibited, ECs exposed to a shear stress of 12dyne/cm^2 for 24h show significantly higher YR compared to ECs without LatB treatment. Higher concentration of 60nM LatB treatment completely inhibit the actin cap formation, nuclear stiffening, and the export process of YAP (Figure 2G).

We next revealed the key roles of actin cap and nuclear mechanics by multidimensional analysis. We found that ECs with lower nuclear stiffness and less actin cap formation have a tendency for YAP nuclear localization (Figure 2H). In contrast, the YAP nucleocytoplasmic shuttle trend failed to be distinguished by other factors, including shear stress magnitude, shear time, and polarity of conventional fibers, as depicted by the standard deviation of the polarity frequency distribution. In addition, we performed the Multiple correspondence analysis (MCA) of these factors. The YR shows high negative correlations with both Brillouin shift (r=-0.95) and actin cap present cells (r=-0.86) instead of the flow conditions and conventional fibers.

Similar to previous studies[2,22], we also found that actin cap has a significant impact on nuclear morphology under shear stress (Figure S2B). As the coupling of actin cap and nuclear mechanics appears to determine YAP localization, we consider these cellular components may mechanically affect the nuclear deformation, and drive

changes in YR. To the end, we applied the theoretical modeling to examine in detail how this coupling determines shear stress mechanotransduction process and determines nuclear deformation and thus regulates YAP nucleocytoplasmic shuttling.

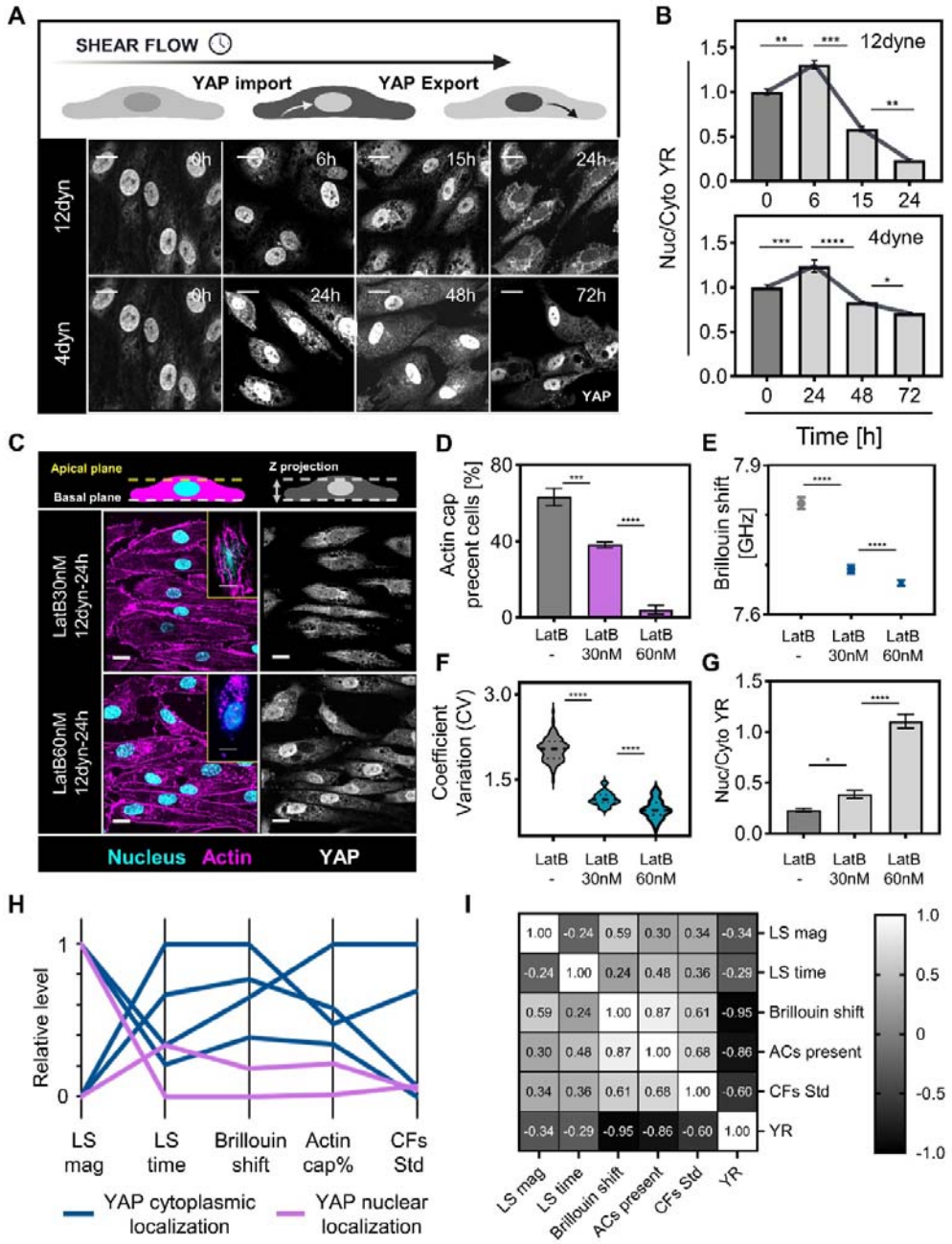

Figure 2. YAP localization is associated with the coupling of actin caps and nuclear mechanics.

(A) Schematic and representative cells subjected to LS with YAP appears first nuclear localization and then cytoplasmic retention as the flow prolonged in both 12 dyne/cm^2 and 4 dyne/cm^2 conditions. The image is obtained from the reconstruction of immunofluorescence confocal images along the Z-axis. Scale bars, 40μm.

(B) Quantification of YAP ratio (YR) variation under LS of 12 dyne/cm^2 and 4 dyne/cm^2 over flow time (n=3 independent experiments with > 100 cells/condition, *p < 0.05, **p < 0.01, ***p < 0.001, ****p < 0.0001. Error bars represent ±SD).

(C) Representative LatB treated conventional fibers, actin caps, and YAP localization under LS of 12 dyne/cm^2 for 24h. Scale bars, 40μm.

(D-E) Comparation of LatB untreated, 30nM LatB treated, and 60nM treated ECs under LS of 12 dyne/cm^2 for 24 hours in actin cap present cells, Brillouin shift, coefficient of variation (CV), and YR (n=3 independent experiments with > 100 cells/condition in actin cap, CV and YR tests, n=5 independent experiments in Brillouin test, *p < 0.05, ***p < 0.001, ****p < 0.0001. Error bars represent ±SD).

(H) Parallel coordinate charts classified by YAP nuclear localization and cytoplasmic retention states, considering the LS magnitude, LS time, Brillouin shift, actin caps (ACs) present cells, and polarization of conventional fibers (CFs). Brillouin shift and ACs present cells can separate two states of YAP localization rather than other factors (n=3 independent experiments with > 100 cells/condition).

(I) Multiple correspondence analysis (MCA) of LS magnitude, LS time, Brillouin shift, ACs present cells, polarization of CFs, and YR (n=3 independent experiments with > 100 cells/condition), which shows the strong correlation between Brillouin shift, ACs present cells, and YR.

A mechano-chemical model to analyze the flow shear stress transmitted to nucleus regulating nucleocytoplasmic transport of YAP.

The cell dimensionality and shape has shown to play crucial roles in controlling the spatiotemporal dynamics of signaling[32,33]. We therefore created a three-dimensional mechano-chemical model of flow shear transmission with key subcellular components related cell shape and deformation, including the cytoplasm, conventional fibers, actin cap and nucleus (Figure 3A), embedded in a microfluidic channel. The flow shear stress and fluid properties in the microfluidic channel in the model are kept consistent with those in the experiment (Figure S3A, Table S2). To understand and predict the nucleocytoplasmic shuttling of YAP, we considered both the involved biochemical pathways and mechanical transmission. The modulus is divided into three parts: (1) flow-induced activation of RhoA at the plasma membrane and the transmitted stress-activation of RhoA at the focal adhesion, (2) major cytoskeletal dynamics regulation pathways downstream of RhoA, (3) YAP phosphorylation and its nucleoplasmic shuttling processes. The shape of the subcellular components used in the computational model was revealed by immunofluorescence staining with CM-Dil, phalloidin, and DAPI (see Figure 3C). The biochemical pathway is adapted from the recent spatial chemical model[33,34] and converted to a mechano-chemical model by considering the intracellular force and deformation. Each part is described below and the reactions and parameters are explained in detail in Table S1-S2.

Module 1: Flow Shear Stress Sensing.

In this module (Figure 3A, numbered as ①), we describe the early mechanotransduction associated with shear stress, especially RhoA activation. Shear stress stimulates integrins and G protein-coupled receptors at the plasma membrane, activating RhoA[35,36], and transmits into the focal adhesion, facilitating focal adhesion kinase (FAK) phosphorylation, which also activates RhoA.

RhoA activation at plasma membrane. In this model, shear stress is incorporated as a stimulus into the signaling pathway that leads to RhoA activation at plasma membrane with kinetics expressed by Hill equation[37], as follows:

$$R_{a\rho} = R_{\max,\rho}\frac{\tau}{\tau + a}C_{Rho} \tag{1}$$

where $R_{max,\rho}$ is the maximum activation rate due to the shear stress, τ refers to the shear stress magnitude, a is the value of shear stress when the activation rate of RhoA reaches $R_{max,\rho}/2$ estimated based on the previous experimental measurements[38]. C_{Rho} and C_{RhoA} is the concentration of Rho and RhoA, respectively.

RhoA activation downstream of phosphorylated FAK. Aside from activation at the plasma membrane, FAK phosphorylation is another source of RhoA activation at focal adhesion. FAK is known to be activated by the stress stimuli at focal adhesion, which can also be modeled as Hill equation. This event is adapted from the published model[33] and given as:

$$R_{pFAK} = k_f C_{FAK} + R_{\max,pFAK}\frac{\sigma}{\sigma + b}C_{FAK} \tag{2}$$

where k_f is the baseline activation rate of phosphorylated FAK, $R_{max,pFAK}$ is the maximum activation rate due to stress (σ) in focal adhesion, b is the value of stress when the activation rate of FAK is $R_{max,pFAK}/2$. C_{FAK} and C_{pFAK} is the concentration of FAK and phosphorylated FAK, respectively. The RhoA activation rate at focal adhesion is modeled as a function of phosphorylated FAK, as shown in Table S1.

Module 2: Cytoskeleton regulation.

In this module, we simulate the cytoskeletal reorganization, particular the myosin and F-actin dynamics via rho-associated kinases (ROCK), formin mDia1 (mDia), LIM kinase (LIMK) and Cofilin pathways downstream of RhoA (Figure 3B). The dynamic of these components is governed by the diffusion-reaction equation:

$$\frac{\partial C_A}{\partial t} = D_A \Delta C_A + R_A \tag{3}$$

where C_A is the concentration of each component in the cytoplasm, D_A is the diffusion coefficient of A, and R_A represents the reaction rates between the components. We only show the general form of the equation here, and the complete reactions and parameters adapted from recent chemical model[33] are explained in detail in the Table S1 and Table S2.

The combined action of myosin and F-actin determines the mechanical stress transmitted in actin fibers. Activated myosin can bind to actin fibers and exert contractile active stress, as shown in Figure 3A (Label ②), and we model the contractile stress as a force dipole of equal magnitude in opposite directions along the fiber, which is assumed to be a linear function of activated myosin concentration (Table S1), similar to the one described in previous research[24]. Furthermore, passive stress is primarily generated by actin fiber stiffness. Hence, the total stress in actin fiber (σ) is given by:

$$\sigma = E_F \varepsilon_F + k_{act} C_{MyoA} \tag{4}$$

where E_F represents the stiffness of actin fiber, which is determined by strain (ε_F) and F-actin concentration (C_{Factin}). The second term with the product of coefficient k_M and activated myosin concentration (C_{MyoA}) represents the active stress.

We then propose that the dynamic accumulation of conventional fibers increases with increasing F-actin concentration, and the direction of conventional fibers is determined by the diffusion potential of F-actin from the basal surface of the cell to the nuclear membrane. What is unclear, however, is how the actin cap forms when the cell is subjected to shear stress. Based on our experimental results, we used the Hill equation to simplify the interaction between actin cap, flow time and shear stress magnitude by fitting the formation of actin cap with flow time and magnitude (see Figure S3B for the fit).

Module 3: YAP nucleocytoplasmic transport.

Here (Figure 3A, numbered as ③), we considered a set of reactions to reveal YAP nucleocytoplasmic shuttling through the cumulative influence of biochemical and mechanical factors. YAP dephosphorylation depends on actin fiber formation

from F-actin and myosin[13,39], whose rate is modeled as a product of F-actin and myosin[33]. The nuclear localization or cytoplasmic retention of YAP is determined by the export and import rates of dephosphorylated YAP. In this model, the YAP nuclear import rate is set as a function of nuclear membrane strain, which reveals the stretch of nuclear pores, while YAP export rate is modeled as a simple first-order rate[20,21,33]. As a result, the combined YAP transport rate across nuclear membrane ($J_{YAP,NM}$) is given by:

$$J_{YAP,NM} = k_{in} \frac{\varepsilon_{NM}}{\varepsilon_{NM} + \varepsilon_{NM,th}} C_{YAP} - k_{out} C_{YAP_{nuc}} \quad (5)$$

where k_{in} and k_{out} is the first-order constant modulating the rate of YAP nuclear import and export. C_{YAP} and C_{YAPnuc} are the concentration of cytoplasmic and nuclear YAP, and ε_{NM} represents the first principal strain of nuclear membrane, and $\varepsilon_{NM,th}$ is the value of strain when the import rate reaches its half maximum. The deformation of nuclear membrane is determined by the stress transmitted from actin fibers shown in Equation 4 and the nuclear mechanics. The relationships between nuclear stiffness, flow time and shear stress magnitude are fitted from the Young's modulus calculated from the measured Brillouin shift with Hill equation (Figure S3C). The viscosity behavior of the nucleus is described by the Maxwell model, whose relaxation time is chosen as 0.3s[40].

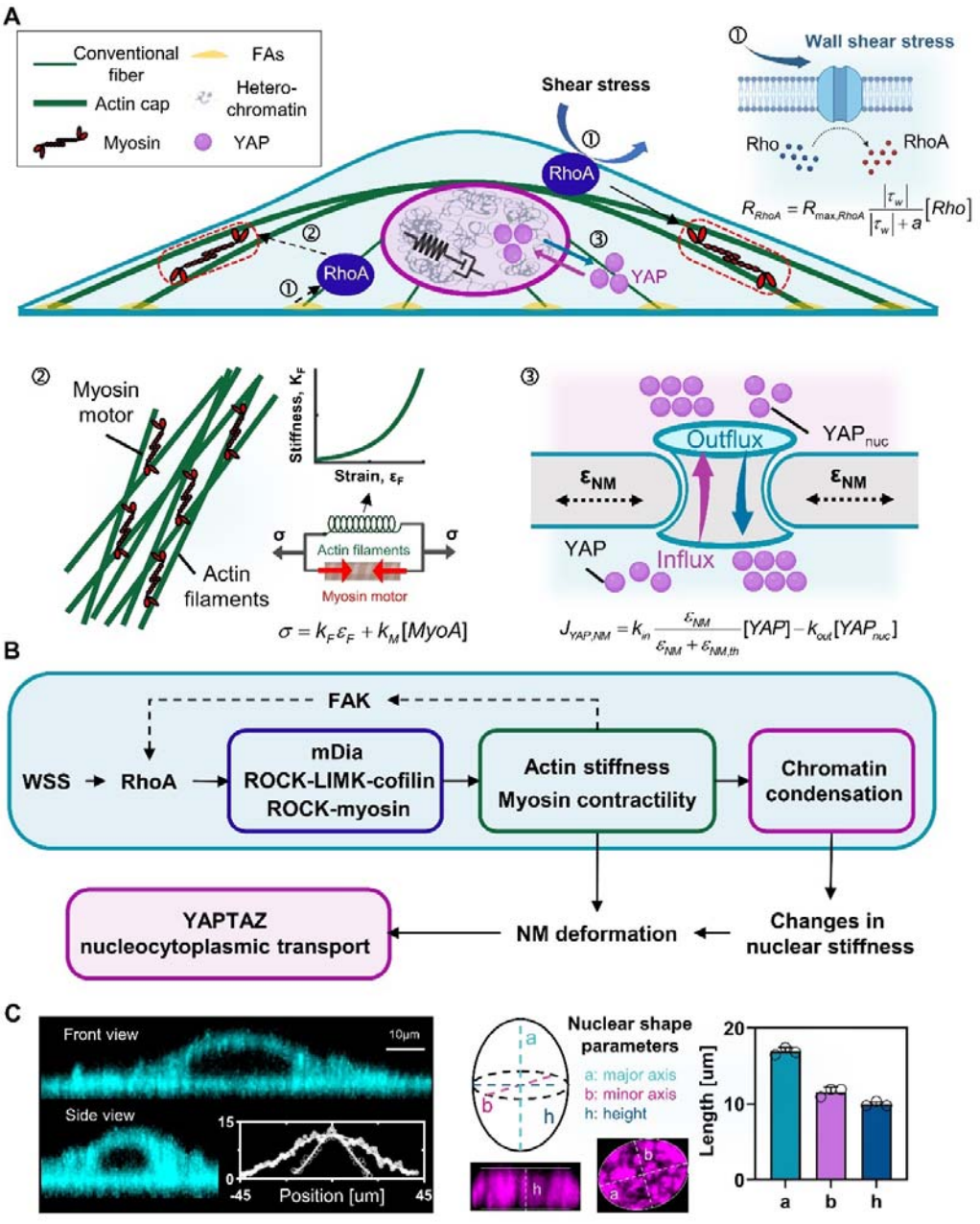

Figure 3. Schematic of the theoretical mechano-chemical three-dimensional model.

(A) The major components considered in the model, including the cytoplasm, conventional fiber, actin cap, nucleus, and biochemical pathways centered on RhoA to regulate the nucleocytoplasmic transport of YAP (FAs indicates the focal adhesion in the figure).

(B) Detailed biochemical pathways involved in the model, including the flow-induced activation of RhoA, major cytoskeletal dynamics regulation pathways downstream of RhoA involving ROCK, mDia, LIMK and Cofilin, and YAP nucleocytoplasmic

transport process.

(C) Geometric parameters obtained from cytoplasm (stained with CM-Dil), fitted by the Gaussian curve, and nuclear images (stained with DAPI), described by the length of major axis, minor axis, and height.

Modelling the spatiotemporal mechanotransduction of shear stress and nucleocytoplasmic shuttle of YAP.

Based on the mechano-chemical model, we first investigate the temporal characteristics of YAP nucleocytoplasmic shuttling through the simulation with a unidirectional flow shear stress of 12 dyne/cm^2 for 86400s (24 hours). The YAP ratio (YR) between the nucleus and the cytoplasm is found to increase rapidly and then decrease gradually (Figure 4A, Video S1), which shows strong agreement with our experimental findings. Furthermore, the model results show a shift in the spatial distribution of YAP. In the static state, YAP in the cytoplasm is symmetrically polarized, concentrated at both ends of the cytoplasm and transported to the nucleus. Under flow shear, the cytoplasm facing the flow direction shows higher YAP concentration compared with the opposite part (Figure 4B), which is consistent with the experimental results (Figure 4C). In addition, the nuclear membrane facing the flow shows overall YAP export, while the opposite part shows YAP import (the concentration gradient field in Figure 4B), echoing the asymmetric distribution of YAP in the cytoplasm.

Then, we reveal the mechano-chemical transduction process of flow shear stress from the actin fibers to the nucleus associated with the YAP nucleoplasmic shuttle. RhoA can be activated both on the cell membrane contact with medium and in the focal adhesion in the basal plane of the cell, which rapidly increases and then gradually decreases as flow prolonged (Figure S4A). In the basal plane, the sites of RhoA and its upstream stress sensitive signal FAK activation would transit from focal adhesions of conventional fibers to actin cap (Figure 4D, Figure S4B-S4C). Through the combined action of the signaling pathways downstream of RhoA, including the mDia, ROCK, LIMK and Cofilin (Figure S4D), the concentration of F-actin and activated myosin in conventional fibers gradually decrease during prolonged flow (Figure 4E). As a result, the averaged stress in conventional fibers gradually decreases due to the combined action of F-actin and myosin (Figure 4F, marked with hollow arrows in Figure 4G). Our model, on the other hand, shows that as the actin cap form during flow, the averaged stress in the actin cap increases significantly with flow time (Figure 4F, marked with solid arrows in Figure 4G). The combined effects of conventional fibers and actin cap is that the nuclear stress is dispersed over the nuclear membrane at the beginning of flow due to the contractile force of conventional fibers (Figure 4H). As the flow prolonged, the nuclear stress is concentrated at the LINC, where the actin cap is attached to the nuclear membrane (solid arrows in Figure 4H), while the stress at other locations significantly reduces. Surprisingly, while the stress in actin-cap associated LINC increases significantly with flow, overall stress in the nuclear membrane decreases (Figure 4F). The deformation of nuclear membrane, described by the averaged strain, increases and then decreases with increasing flow time (Figure 4G, Video S2), corresponding to the change in YR, indicating that nuclear deformation under shear stress plays an important role in the YAP nucleocytoplasmic shuttle process. In addition to the 12 dyne/cm^2 condition, we perform a 72-hours simulation with a shear stress of 4 dyne/cm^2, and the calculated YAP transport process also reproduces the experimental

results and corresponds to the nuclear membrane deformation, which can be found in the Figure S4E.

Next, we examine the coupling effects of actin cap and nuclear mechanics in shear stress transmission and YAP nucleocytoplasmic shuttle by separately inhibiting the formation of actin cap and nuclear stiffening in the model. Simulation predicts that the nuclear stiffening alone (actin cap-, nuclear stiffening+, Figure 4H Quadrant IV) results in the increase of nuclear membrane strain compared to the coupling effects (actin cap+, nuclear stiffening+, Figure 4H Quadrant I), which leads to more nuclear import sites in nuclear membrane and a stronger trend of YAP nuclear localization. The effect of actin cap alone (actin cap+, nuclear stiffening-, Figure 4H Quadrant II) is consistent with but not as significant as the separate effect of nuclear stiffening (Figure 4H). When the two factors are both inhibited (actin cap-, nuclear stiffening-, Figure 4H Quadrant III), the nuclear membrane strain would increase more significantly, which results in higher YAP nuclear concentration. We then use the model to calculate the YR and nuclear membrane strain temporal dynamics, and found that inhibiting actin cap and nuclear stiffening can both decrease YAP export and the nuclear membrane strain decreasing tendency under long time flow. It is worth emphasizing that when these two factors are suppressed simultaneously, the decreasing trend of YR and nuclear membrane strain will completely disappear (Figure 4I-4J).

These simulations reveal insights into the mechanism by which the coupling of actin cap and nuclear mechanics dominates nuclear deformation, and regulating the YAP nucleocytoplasmic shuttle. Initially, the cell has low nuclear stiffness and more conventional fibers rather than actin caps, leading to increased nuclear membrane strain and YAP nuclear import. As nuclear stiffness increases and actin cap forms during flow, the nuclear membrane strain decreases, resulting in YAP export from nucleus.

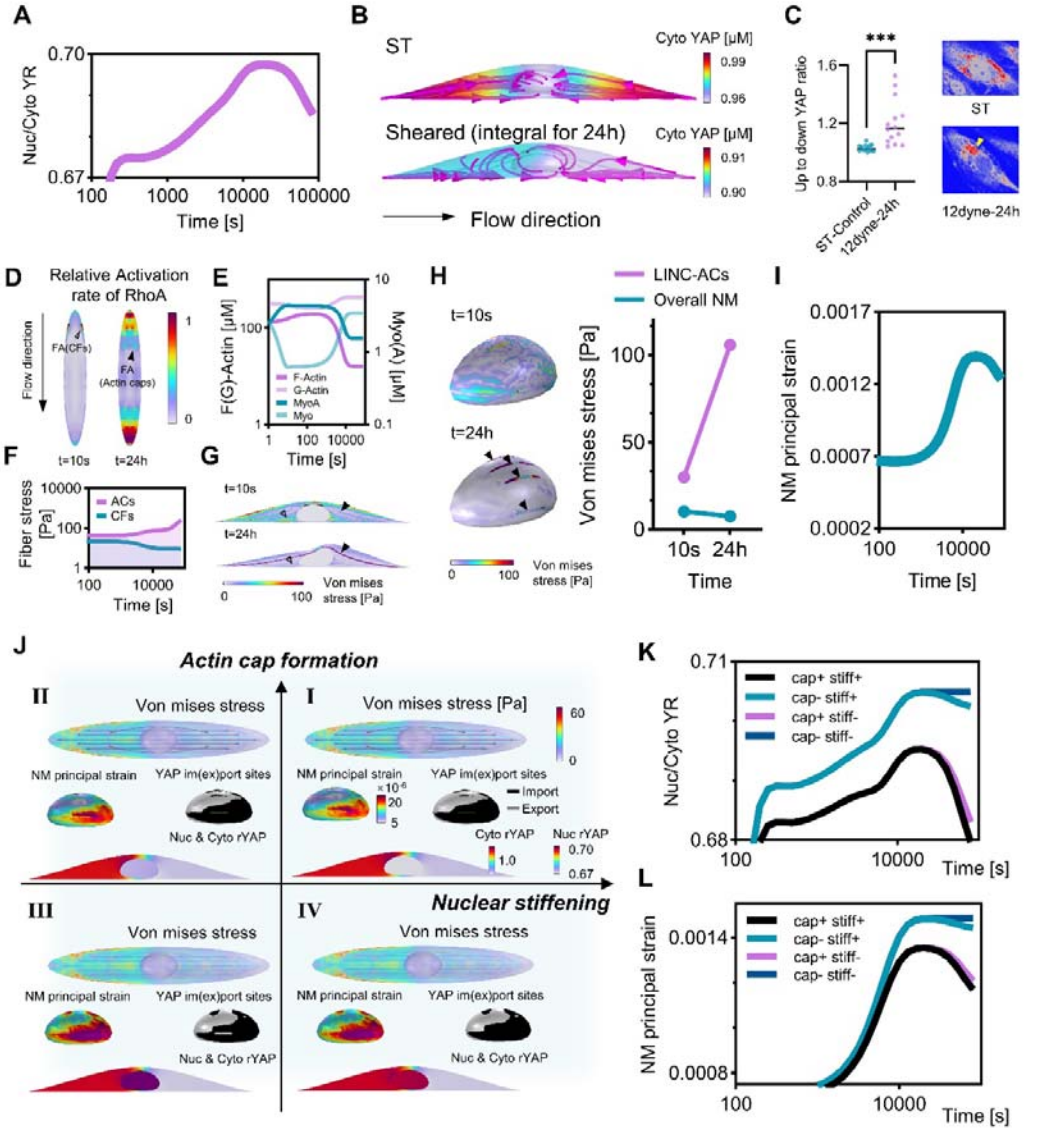

Figure 4. Spatiotemporal shear stress mechanotransduction and YAP distribution mediated by the interaction between actin cap and the nuclear mechanics.

(A) Predicted YAP ratio (YR) between nucleus to cytoplasm under LS of 12 dyne/cm^2 in 24 hours.

(B) Predicted YAP spatiotemporal distribution in ST control and LS of 12 dyne/cm^2 for 24 hours, and the streamlines refer to the YAP transport directions in cytoplasm.

(C) Experimental YAP spatiotemporal distribution in ST control and LS of 12 dyne/cm^2 for 24 hours. Arrowhead indicates the unsymmetrically polarized spatial distribution of YAP in cytoplasm under LS.

(D) The relative RhoA activation rate normalized by its maximum value at the initial (t=10s) and end state (t=24 hours) of flow stimuli.

(E) Simulated spatial averaged concentration of F-actin, G-actin, myosin, and activated myosin during LS.

(F) The averaged Von mises stress in the conventional fibers and actin cap during LS.
(G) Von mises stress distribution inside the cell at the initial (t=10s) and end state (t=24 hours) of flow stimuli. The deformation is visualized and expanded by a factor of 100.
(H) Nuclear forces distribution in the actin cap-associated LINC (marked with arrowhead) and nuclear membrane (NM). The stress at actin cap-associated LINC increases as LS prolonged, while the stress at the overall NM significantly reduces.
(I) The dynamics of nuclear deformation under LS, described by the principal strain of nuclear membrane (NM).
(J) Individual effects of actin cap and nuclear stiffening in shear stress mechanotransduction and YAP nucleocytoplasmic shuttle (t=86400s, Quadrant I: actin cap+, nuclear stiffening+; Quadrant II: actin cap+, nuclear stiffening-; Quadrant III: actin cap-, nuclear stiffening-; Quadrant IV: actin cap-, nuclear stiffening+).
(K-L) The explicit effects of actin cap and nuclear stiffening in surface-averaged nuclear deformation and YR under LS.

The mechano-chemical behaviors involved in shear stress mechanotransduction

After predicting the effects of the actin cap and nuclear mechanics on shear stress mechanotransduction and the YAP nucleocytoplasmic shuttle, we attempt to assess the reliability of the model by comparing other predicted mechanical and chemical behaviors with experimental evidences. From the mechanical perspectives, during the flow, the height of the nucleus decreases owing to actin cap compression, with a slow rebound after 15 hours (Figure 5A). Consistent with this, the model shows that the nucleus's z-direction deformation will initially rise and then progressively recover (Figure 5B). In addition, we compare the simulated actin fiber reorganization to F-actin immunofluorescence staining. We found that the actin fibers obtained from the model exhibit polar remodeling in the basal plane facing the flow, and form actin cap in the cell apical plane, which is compatible with the experimental results (Figure 5C). From the biochemical perspectives, the spatial distribution of reaction flux and concentration of cytoplasmic components depends not only on the geometric curvature illustrated in previous research[32,41], but also on the direction of external shear stimuli dependence (Figure 5C). This prediction suggests that cell shape still play a role in information processing under shear stress[42]. Furthermore, we examine the relationships among the spatial averaged concentrations of the signaling components involved in the model. The model can reproduce the correlation of cascade signaling molecules in the three pathways shown in Figure 3B: positive correlations between RhoA and its downstream activated ROCK and myosin, positive correlations between RhoA and its downstream mDia and F-actin, and the correlations between RhoA, activated ROCK, LIMK, cofilin and F-actin (Figure 5D).

Since previous studies pointed out that YAP nucleocytoplasmic shuttle is determined not only by mechanical cues but also by biochemical regulations centered on YAP phosphorylation, we further investigate the role of chemical signaling in YAP transport. The model shows that as the unidirectional flow prolonged, the ratio of phosphorylated YAP (pYAP) to dephosphorylated (YAP) gradually increases (Figure 5F), *i.e.*, the YAP activity received inhibition by unidirectional shear stress, which is consistent with multiple published experimental studies[11,17]. In addition, we artificially inhibited mechanosensitive nuclear transport of YAP to verify whether the nuclear membrane deformation-related YAP nucleocytoplasmic shuttle we found originated primarily from an increase in deactivated pYAP. As shown in Figure 5G, when the mechanosensitive nuclear transport of YAP is completely inhibited, YAP becomes a freely diffusing molecule and rapidly enters and then exits the nucleus up to a stable level, and the whole process will be completed within 3 hours (Figure 5G). The time scale cannot correspond to the results of experimental and mechano-chemical model. In addition, when compared to the combined regulation of chemical and mechanical factors, the idealized stable YR level in the non-mechanosensitive model would be substantially higher (Figure 5G). As a result, in the absence of mechanical regulation, YAP may import the nucleus more quickly and violently, followed by a slight export to a stable value under the action of the free diffusion potential, emphasizing the dominate roles of mechanical regulation in YAP transport.

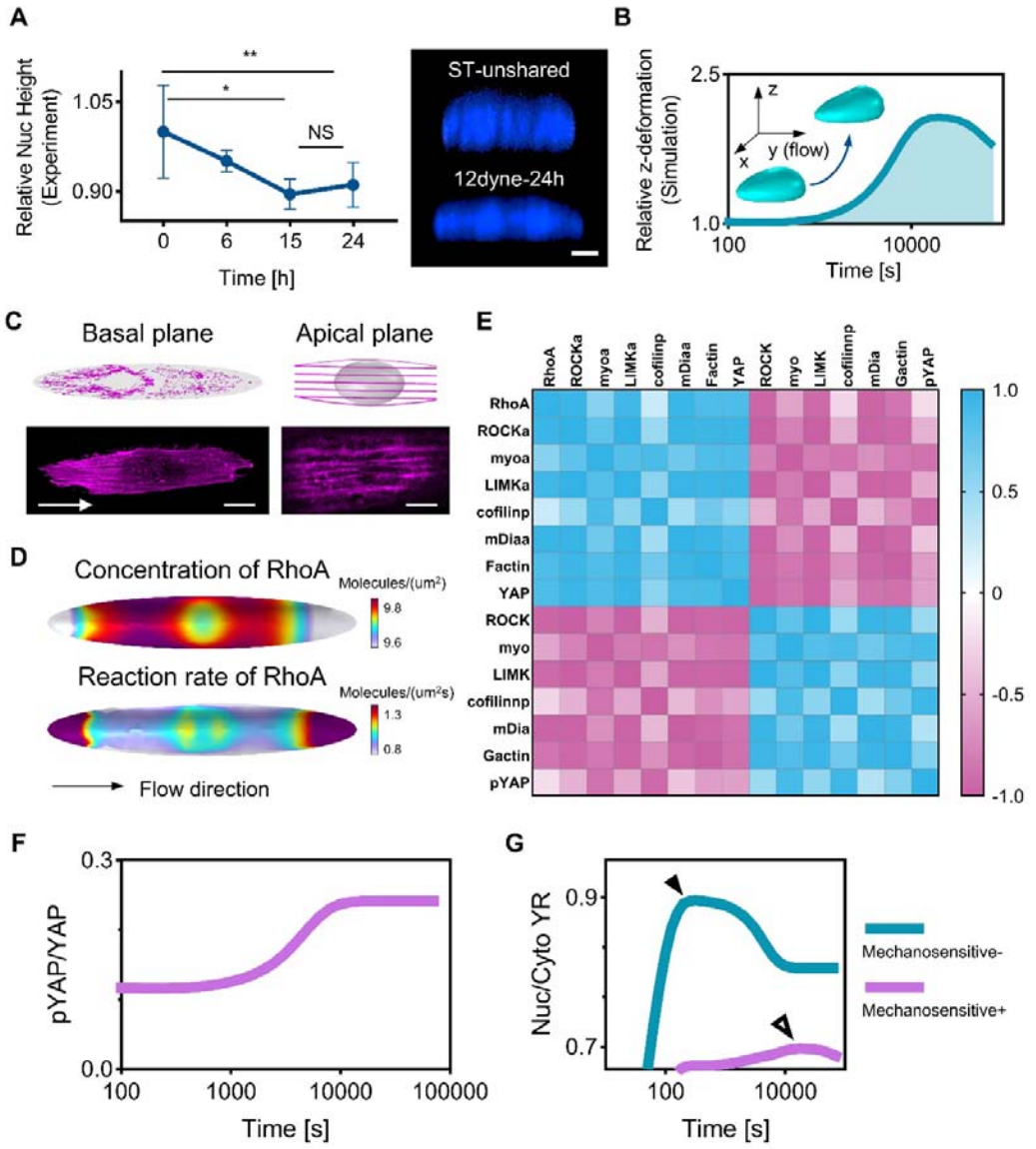

Figure 5. The prediction of mechano-chemical behaviors involved in shear stress mechanotransduction.

(A) Experimental measured nuclear height changes under LS (n=3 independent experiments with > 100 cells/condition; NS: $p > 0.05$, *$p < 0.05$, **$p < 0.01$. Error bars represent ±SD)

(B) Predicted nucleus's z-direction deformation under LS.

(C) Experimental and predicted organization of actin filaments, including conventional fibers in the basal plane and actin cap in the apical plane.

(D) The spatial distribution of RhoA concentration and reaction rate at cell membrane under LS.

(E) Multiple correspondence analysis (MCA) of the concentrations of cascade signaling pathways involved in the model, including RhoA, and the activated

(inactivated) ROCK, myosin, LIMK, cofilin, mDia, actin, and YAP.
(F) The activation of YAP, described by the ratio of pYAP to YAP, regarding to LS time.
(G) The comparation of artificially fully biochemical regulation of YAP and mechan-chemical regulation of YAP.

Actin cap and nuclear mechanics interaction regulates the oscillating flow mechanotransduction.

Contrary to laminar flow (LS), endothelial cells exposed to oscillatory shear stress (OS) results in a pro-inflammatory phenotype, which is associated with the development of diseases such as atherosclerosis and thrombosis[43-45]. OS has been found to consistently induce YAP nuclear localization in vascular and lymphatic endothelial cells at 12, 24 and 48 hours[17,46], which contrasts with the transient nuclear import and then export of YAP in ECs exposed to LS. In addition to the biochemical regulation of YAP activation via signaling pathways such as RhoA and C-Jun N-Terminal Kinase (JNK)[11,17], we speculate that the coupling of actin cap and nuclear mechanics also has an important role in the regulation of YAP nucleocytoplasmic shuttle under OS.

Similar to the previous studies, we found that YAP is continuously located in the nucleus, resulting in the high ratio of nucleus to cytoplasm YAP (YR) from 6 to 24 hours at 1Hz oscillatory shear stress of 0 ± 12dyne/cm^2 (Figure 6B). In addition, we found that actin cap formed gradually and reached stability after 15 hours under the action of OS (Figure 6C). However, the percentage of cell with actin cap and the polarization of conventional fibers is much less compared to the action of LS with the same shear stress magnitude of 12 dyne/cm^2 (Figure 1C, Figure S1A). In contrast to the nuclear stiffening observed in LS, nuclear stiffness of ECs exposed to OS decreases significantly after 15 hours (Figure 6D) and is accompanied by a significant decrease in chromatin heterogeneity (Figure 6E). With the theoretical model, we analyze the alteration in the nuclear membrane deformation under OS by ideally shortening the actin cap formation and nucleus softening process in 24 hours (86400s) into the simulation of 8.64s. The changes in both actin cap formation and nucleus stiffness are described by the Hill equation (Figure S3B-S3C), with the former increasing and the latter decreasing with flow time (Figure 6F). The model predicts that due to nucleus softening and less actin cap formation compared to LS, nuclear membrane strain increases significantly in each oscillating period, which is corelates with the external OS. The large deformation of nuclear membrane in each period would facilitate the nuclear import of YAP, corresponding to the experimental observation of high YR under OS stimuli (Figure 6G). In addition, we used the computational model to artificially promote the formation of actin cap and inhibit nuclear softening during OS, and found that both the nuclear membrane strain and the YR decrease as flow prolonged (Figure S4F).

In conclusion, ECs form less actin cap under OS compared to LS and the nucleus softens, leading to a large oscillating fluctuation in nuclear membrane deformation and promoting YAP entry into the nucleus. This mechanical mechanism together with

the other biochemical cues of YAP activation may determine the nuclear localization of YAP under OS.

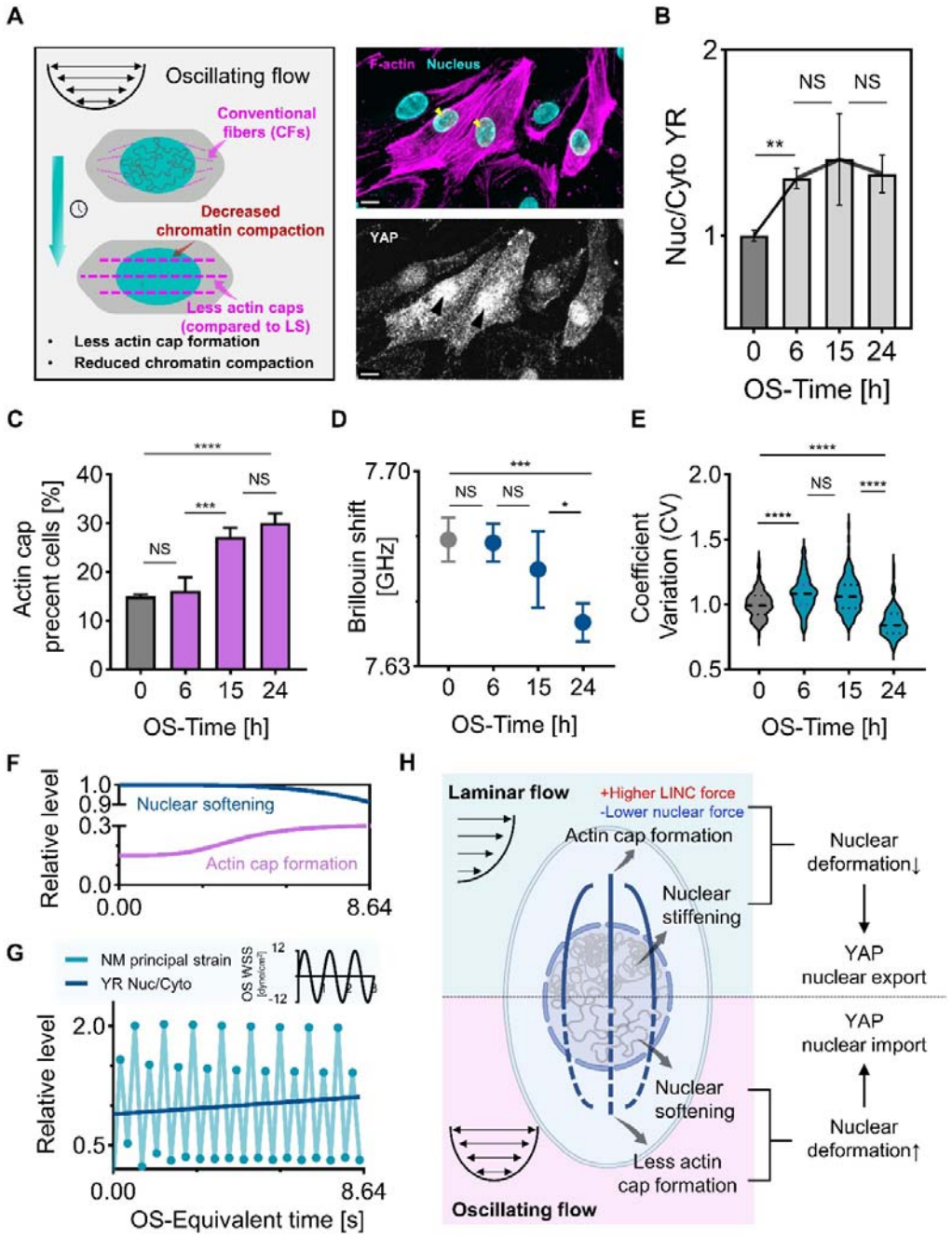

Figure 6. The actin cap and nuclear mechanics coupling under oscillatory shear stress.

(A) Schematic of cell subjected to oscillatory flow with actin cap formation and YAP nuclear localization. Scale bars, 10μm (Arrowheads in yellow point to the actin cap, and arrowheads in black point to the YAP nuclear localization).

(B) YR variation under OS of 12 dyne/cm^2, 1Hz over flow time (n=3 independent experiments with > 100 cells/condition; NS $p > 0.05$, **$p < 0.01$. Error bars represent ±SD).

(C-E) Time-dependent variations in actin cap present cells, Brillouin shift, coefficient of variation, (n=3 independent experiments with > 100 cells/condition in actin cap, CV tests, n=5 independent experiments in Brillouin test, *p < 0.05, ***p < 0.001, ****p < 0.0001. Error bars represent ±SD).

(F) Relative changes in actin cap and nuclear stiffness with OS time applied to the model.

(G) The deformation of nuclear membrane (NM) under OS shows an oscillating trend with a period consistent with the external stimulus. YR ratio of nucleus to cytoplasm increases as OS prolonged. The NM principal strain and YR are both normalized by their averaged values.

(H) Schematic diagram of cells exposed to LS or OS. Short term shear stress has no effects on actin cap and chromatin condensation and nuclear stiffness. Prolonged LS leads to a significant formation of actin cap and chromatin condensation and nuclear stiffness, and OS stimuli leads to a less formation of actin cap accompanied by a decrease in chromatin condensation and nuclear stiffness. Actin cap formation and nuclear stiffening decrease the nuclear deformation, facilitating the nuclear export of YAP.

Discussion

Combining biological experiments and computational studies, we found that nucleocytoplasmic shuttling of YAP under flow shear stress is governed by the nuclear deformability, which is controlled by the interaction between the actin cap formation and altered nuclear mechanics. Through the proposed mechano-chemical model, we demonstrate that the formation of perinuclear actin cap with flow concentrates the transduction of force in the LINC and reduces the overall nuclear deformation, similar to the recently identified mechanical function of actin cap when fibroblast cells are subjected to substrate stretch[2]. Furthermore, we revealed the stiffening of nuclear stiffness also decreases the deformation induced by transmitted force. Due to the differences in actin cap formation and nuclear stiffness alteration in ECs under various shear stress stimuli, the nucleoplasmic shuttle process of YAP is spatiotemporally varied. Under short time unidirectional laminar shear stress (LS), the actin cap and nuclear stiffening are absent, resulting in large nuclear deformation partly caused by mechanotransduction of basal conventional actin fibers. The nuclear deformation in turn regulates YAP nuclear localization, which is in consistent with the idea of nuclear pore complex opening mediated by nuclear tension[20,21]. Under prolonged LS, the actin cap as well as nuclear stiffening are significantly formed, leading to reduced nuclear deformation and YAP nuclear export (Figure 6H). In contrast, in the presence of oscillatory shear stress (OS), actin cap forms slightly with nuclear softening, leading to the periodic high value of strain in oscillation and YAP nuclear import. Taken together, our results demonstrate that flow-induced reorganization of actin cap and nuclear mechanics is an essential factor regulating the seeming contradictory cytoplasmic retention or nuclear localization of YAP under diverse shear stress conditions.

Several canonical experimental techniques have been developed to assess the mechanical properties of nucleus, such as atomic force microscopy (AFM)[47] and micropipette[48]. To directly assess cells embedded in microfluidic chips and reduce the impact caused by measurement contact and cell nucleus separation process of the traditional methods, we used a novel optical technique, Brillouin microscopy, capable of measuring nuclear stiffness in a label-free, non-contact and non-invasive manner. To verify the reliability of Brillouin microscopy, we quantified the degree of chromatin compaction and found a strong correlation with the nuclear stiffness, which is consistent with the published well-proven conventional mechanical measurements[28,49,50]. In addition, it has been reported that the degree of chromatin compaction is associated with the localization of YAP[51,52]. For example, epithelial cells exposed on convex curvature show an elevated nuclear presence of YAP and less condensed chromatin, while the nucleus on concave curvatures contains more condensed chromatin with cytoplasmic YAP[53]. These experimental observations of YAP transport induced by variable mechanical cues might be partially driven by the alteration of nuclear stiffness induced by condensed chromatin.

Since the polymerization of F-actin is accompanied by changes in chromatin condensation[54,55], it is difficult to control the formation actin cap and nuclear stiffness

individually by experimental methods. Therefore, we used the mechano-chemical model of shear stress transmission to investigate the respective effects of actin cap and nucleus stiffness on YAP transport. We also simultaneously removed the formation of actin cap and nuclear stiffening process and predicted that the nuclear export process of YAP is completely inhibited under prolonged LS, which is in agreement with our experimental results of treating ECs with LatB which both affects the actin cap and nuclear stiffness. It has been observed experimentally that actin cap formation under substrate stretching leads to YAP nuclear localization[56], which might be due to the calcium-dependent chromatin decondensation[29] and nuclear softening process during stretch, similar to what we explored when cells are subjected to OS. This interpretation can be supported by the recent evidence that when cells are exposed to prolonged stretching, the nucleus stiffens and leads to the YAP nuclear export again[57].

Our finding shows that nuclear deformation caused by actin cap and nuclear mechanics interaction under shear stress might be a Hippo-independent YAP regulation mechanism. This novel mechanism includes not only previously identified shear stress activation of YAP, but also actin cap, nuclear stiffness, and nuclear deformation. It was recently noted that force is capable of regulating nucleocytoplasmic transport of many transcriptional regulators other than YAP (*e.g.*, MRTF-A, β-catenin, MyoD, *etc.*), and thus the interaction of actin cap and nuclear mechanics may be a retention mechanistic regulatory mechanism under shear stress, independently of any specific signaling pathway[20,21]. This link between actin cap, nuclear stiffness, nuclear deformation, and YAP localization under shear stress could provide therapeutic strategies for diseases associated with pathological flow stimulations, such as atherosclerosis and cancer[7-11]. Furthermore, since the interaction of the actin cap with the nucleus also dominates stem cell differentiation[58], a clearer understanding of mechanistic YAP regulation may also provide a guiding strategy, especially for flow-controlled stem cell differentiation[39,59,60].

Acknowledgments

This work was supported by the National Natural Science Research Foundation of China (grant no. 11827803, 31971244, 31570947, 32071311, and U20A20390), the Fundamental Research Funds for the General Universities (KG16186101) and the 111 Project (B13003).

Author contributions

T.M, X.L., and H.S. conceived, designed, and led the interpretation of the project. T.M and X.L. led the development of the overall model and theory. T.M., S.L., and F.W. carried out the bio-optical measurements of cells. H.S., C.G., Z.L., D.Z., X.Z., K.L., K.H. L.W. carried out the biological and microfluidic experiments. M.W. provides the biological sample of cells. Y.H., W.H., X.C., and X.D. provided guidance on analyzing and interpreting the resultant of bio-optical measurements and the

computational models. T.M., X.L., P.W., and Y.F. designed the experiments. All authors contributed to the writing of the manuscript.

Declaration of interests

None

METHODS

KEY RESOURCES TABLE

REAGENT or RESOURCE	SOURCE	IDENTIFIER
Antibodies		
Mouse polyclonal anti-human YAP	Santacruz	Cat# sc-101199
Alexa Fluor 488 goat anti-mouse IgG	Abcam	Cat# ab150077
YF594-Phalloidin	US Everbright Inc	Cat# YP0052L
DAPI	Yogoo	Cat# GY17510
Cell Tracker CM-DiI	Amresco	Cat# C4060S
Biological samples		
The umbilical cord of a newborn	Chinese People's Liberation Army General Hospital Fourth Medical Center	http://www.pla304hosptal.com
Chemicals, peptides, and recombinant proteins		
Collagenase type 2	Invitrogen	Cat#17101015
25% trypsin-EDTA	Invitrogen	Cat#25200072
Fetal calf serum	Invitrogen	Cat# no. 10270-106
Fibronectin	Corning	Cat#356008
4%Paraformaldehyde	Biosource	Cat#Y-10034
Endothelial cell medium	ScienceCell	Cat#1001
Triton X-100	Solarbio	Cat#T8200
5%BSA	Solarbio	Cat#SW3015
DMSO	Sigma-Aldrich	Cat# D2650-5X5ML
Latrunculin B	Abcam	Cat# ab144291
Photoresist (SU8-2075)	MicroChem	Cat# wsn2705
Polydimethylsiloxane	Dow Corning	Cat# SYLGARD 184
Deposited data		
Code for three-dimensional mechano-chemical modeling of cell exposed to shear stress	This paper	N/A
Software and algorithms		
Leica Application Suite software	Leica	LAS X version 2.0.0.14332
ImageJ	Schneider et al.[61]	https://imagej.nih.gov/ij/
Matlab	MathWorks	https://www.mathworks.com/products/matlab.html
COMSOL Multiphysics	Comsol, Inc	https://www.comsol.com/

METHOD DETAILS

Cell culture. Human umbilical vein endothelial cells (HUVECs) were isolated from newborn umbilical cords, as detailly described in our previous study[62]. Informed consent was obtained for each donor and all processes were approved by the Beihang University Ethical Committee. The primary HUVECs were cultured in endothelial cell medium (ECM, ScienCell) with 5% FBS, 1% endothelial cell growth supplement (ECGS), and 1% penicillin/streptomycin solution, and incubated at 37 °C under 5% CO_2. The cells were fed one time a week with a complete change of fresh culture medium and used between 2 to 6 passages.

Microfluidic Vascular Chip Fabrication. The microfluidic device was fabricated out of polydimethylsiloxane (PDMS, Sylgard 184, Dow Corning) using standard soft lithography (Figure S5A-S5B). The microfluidic chip is made up of three layers containing PDMS channel layer, thin PDMS membrane middle layer and glass coverslip supporting layer. To make the PDMS channel layer, PDMS prepolymer with a 10:1 (w/w) mixture of PDMS base and curing agent was casted against a photolithographically prepared master with a designed microchannel made of photoresist (SU8-2075, MicroChem) on a silicon wafer, and then cured for 2 hours in an 80 □ dry oven. After separation from the wafer, one media injection port and one media efflux ports were punched out of the molded channel layer using a 3.5 mm biopsy punch, respectively. The middle layer of thin PDMS membrane was produced by spin-coating PDMS prepolymer on silanized silicon wafers at 3500 rpm for 50s on a spin coater and baking on a hot plate at 180 °C for 30 minutes. The channel layer and thin PDMS membrane were cleaned with dusting compressed air tank, and then treated with oxygen plasma for 50 s to form covalent bonds between them. They were then placed in the oven for 10 minutes to strengthen the bonding. Finally, the device stripped from silicon was bonded to the glass coverslip in the same manner of oxygen plasma treatment.

Before cell seeding, microfluidic chips were sterilized for 1 hour by ultraviolet irradiation in the clean bench, and then the culture channels were coated with 125 μg/ml fibronectin. ECs were seeded into the channel and attached to the membrane surface for 1 hour at 37°C under static condition. In all experiments, the density of ECs was controlled at ~500 cells/mm^2 to avoid the effects of cell density changes on YAP localization. The attached cells were then filled with ECM by two 3/32" barbed female Luer adapters (Cole-Parmer) inserted into the medium injection ports to provide nutrients, which the medium in the Luer adapter was changed every 12 hours.

Control of Flow Shear Stress in Microfluidic System. The control of fluid flow system in the present study consisted of one micro-syringe pump (Lead Fluid), one electromagnetic pinch valve and a reservoir, which was used in our recent study[62]. Medium flow was provided synchronously by the programmable micro-syringe pumps. The electromagnetic pinch valve was used to switch the fluid flow between injecting into the microfluidic chip and withdrawing from the reservoir. To introduce flow into the microfluidic device, a sterile polypropylene barbed elbow fitting (1/16″,

Cole-Parmer) connected to Teflon tubing was inserted into the inlet port of cell channel. The fluid flow was introduced from the chip's outlet port into the reservoir and later withdrawn to the micro-syringe pump to create a highly efficient circulation system.

For the unidirectional laminar flow (LS), stable waveforms are used in the control system. Luminal shear stress in the endothelial cell culture channel was determined according to the equation: $\tau = 6\mu Q/Wh^2$, where τ is shear stress (dyne/cm^2), μ is the viscosity of the cell medium (8.8×10^{-4} Pa·s), Q is the flow rate across the endothelial cell culture channel (ml·s^{-1}), h is the channel height (designed as 60 μm and measured after fabrication) and W is the channel width (designed as 600 μm). Cells were then exposed to 4 dyne/cm^2 for 24, 48, 72 hours and 12 dyne/cm^2 for 1, 6, 15, 24 hours. For oscillatory flow, the microfluidic chips were connected to the circulation control system input a sinusoidal waveform often used for oscillating flow. The waveform of flow rate was also measured by flow sensor (ElveFlow, Figure S5C). ECs were exposed to oscillatory shear stress (OS, 0 ± 12 dyne/cm^2, 1Hz frequency) for 1, 6, 15, 24 hours.

Immunofluorescence and Confocal Microscopy. Cells were fixed in 4% paraformaldehyde (PFA) for 10 minutes, permeabilized with 0.1% Triton X-100 in PBS at room temperature, and blocked in 5% bovine serum albumin (BSA) for 1h. Cells were then treated by primary antibodies at 4°C overnight, and incubated with appropriate secondary antibodies for 2 hours at room temperature. Specifically, YAP was stained mouse polyclonal anti-human YAP (sc-101199, 1:200, Santacruz) and Alexa Fluor 488 goat anti-mouse IgG H&L (ab150077, 1:200; Abcam). Phalloidin labeled with Alexa Fluor 488-conjugated phalloidin (YP0052L, 1:200; EVERBRIGHT) was used together with secondary antibodies. Nucleus were stained with 4′,6-diamidino-2-phenylindole dihydrochloride (DAPI; 1:1000; Sigma-Aldrich) for 10 min. For CM-DiI staining, the CM-DiI storage solution (C4060S,1:1000, Amresco) was added to the microfluidic device, and incubated for 5 minutes at 37□ in a carbon dioxide incubator. The cells in the microfluidic device were then incubated in a refrigerator at 4□ for 15 minutes and washed with PBS solution for three times. All fluorescence images were collected by a laser scanning confocal microscopy (SP8X; Leica) with Leica Application Suite software (LAS X version 2.0.0.14332), using objective lens (NA = 0.6, magnification: 40×).

Latrunculin B Treatment. We achieved actin caps disruption in ECs by submerging cells in 30nM to 240nM Latrunculin B (LatB, Abcam) dissolved in DMSO solution (Sigma-Aldrich). To minimize the effects of LatB on conventional fibers rather than the actin cap, the time of LatB treatment was controlled under 1 hour. In flow experiments, LatB is added to the ECM medium at the corresponding concentration.

Brillouin Microscopy Setup. A custom Brillouin microscopy was built to obtain biomechanical images of endothelial cells cultivated in the microfluidic vascular chip based on the recent protocol[63,64]. A 10mW single longitudinal mode CW 532nm laser

(MSL-FN-532, CNI) was utilized as the light source to probe Brillouin scattering. The laser beam was focused into the center of the microfluidic channel by an objective lens (OBJ, NA = 0.6, magnification: 40×), providing a spot size of ~0.5μm (transverse) and ~2μm (axial). The backward scattered light was collected by the same OBJ, reflected at the polarized beam splitter (PBS), and coupled to the single-mode fiber (SMF). The microfluidic vascular chip was equipped on a 2D translational stage with 0.5μm resolution (SC-200, KOHZU Precision) to perform fast two-dimensional scanning.

The customized Brillouin spectrometer (Figure 1D) has two stages with orthogonally oriented VIPA (Free Spectral Range 30GHz, LightMachinery). The light coming out of the fiber is coupled in the vertical direction to VIPA 1 through cylindrical lens CL1, and the spectral pattern output from VIPA 1 is projected onto mask 1 (M1) through cylindrical lens CL2. Then, spherical lens L1 couples the pattern on M1 to VIPA 2 in the horizontal direction, and spherical lens L2 projects the spectral pattern at the output of VIPA 2 onto mask 2 (M2). The spectral pattern is imaged by the CMOS camera (iXon, Andor) after relating through a 4f system consisting of spherical lenses and spatial filter[65], the spectral pattern is imaged by the CMOS camera (ORCA-Fusion, Hamamatsu). To improve the extinction of the spectrometer, linear variable ND filters (filters 1 and 2, not seen in Figure 1D) were put immediately after the VIPA, transforming the intensity profile of the VIPA pattern from exponential to Gaussian. A Matlab software was developed to drive both the stage and the camera simultaneously, and output the Brillouin shift data by automatically least square Lorentzian fitting the Brillouin spectra. To obtain the Young's modulus of the nucleus used in the computational model from the measured Brillouin shift (ν_B), we first calculated the longitudinal modulus M' according to[63]:

$$M' = \frac{\rho \lambda^2 \nu_B^2}{4n^2}$$

where ρ refers to the density of the nucleus (ρ=1350kg/m^3), and λ is the wavelength of the incident light which equals to 532nm, n is the refractive index of the nucleus (n=1.38). Then, we transformed the longitudinal modulus M' to the Young's modulus E based on the log-log liner relationship[66]:

$$\log\left(M'\right) = a\log\left(E\right) + b$$

where a and b are the constant coefficients and equals to 0.081 and 9.37 according to the published study[66].

Preparation and mechanical measurements of gelatin methacryloyl (GelMA) Hydrogels. At 80 °C, different amounts of freeze dried GelMA macromer were dissolved in DPBS containing 0.5% (w/v) 2-Hydroxy-4'-(2-hydroxyethoxy)-2-methylpropiophenone (Sigma-Aldrich) as photoinitiator, yielding final GelMA concentrations of 5%, 7.5%, 15%, and 20% (w/v). After pipetting the prepolymer solution into a glass mold, it was subjected to 1000 mw/cm^2 UV radiation (360-480 nm) for 180 seconds. In the uniaxial

compression test, samples were made as cylinder specimens with diameter of 4 mm and thickness of 8 mm. Brillouin microscopy was then used to assess the stiffness of the samples, which was compared to the Young's modulus derived from compression tests.

Simulation Procedure of the Computational Model. To investigate the mechano-chemical interaction among subcellular components under shear stress stimuli, a 3D finite element model (FEM) was constructed that connected fluid flow in the microfluidic channel, mechanical deformation, and biochemical cascade signaling transfer of adhering single cells. In this study, numerical simulations were carried out using the finite-element package COMSOL (Burlington, MA), which provides multi-physics coupling of the laminar flow, the solid mechanics, and the diluted species transport components. The model's extracellular fluid properties were set to match our experimental setup in the microfluidic device. The cellular model was composed of three deformable components: cytoplasm, nucleus, and actin fibers (both conventional fibers and actin caps), the mechanical properties of which had previously been documented. Our experimental results were used to fit the flow time-dependent changes in nuclear stiffness and actin cap formation (Figure S3B-S3C). The biochemical cascade signaling pathways were adapted from the previous numerical models of basal stiffness-mediated YAP transport[24,33], whose details can be found in Table S1 and Table S2.

Tetrahedral mesh was used to mesh the entire geometric model. To ensure that grid nodes are aligned and non-overlapping, several subdomains with varying spatial sizes and transport properties shared topology. In the boundary layer, the element adjacent to the endothelial membrane surface was set to be 0.15μm, and gradually grew over 5 layers. As the boundary conditions for the fluid parts, the inlet velocity of the microfluidic channel was set up consistent with the experimental setup to ensure the shear stress magnitude of 4 dyne/cm^2, 12 dyne/cm^2, and 0 ± 12 dyne/cm^2 (Sine function with the frequency of 1 Hz). The outlet pressure of the microfluidic channel was set to be a zero pressure. As the boundary conditions for the solid parts, the bottom of the compartment model was fixed in all directions. The surfaces of nucleus and actin cap are in contact with each other. The contact conditions were assumed as tied-type contact methods to mimics the present of LINC. The Fluid-Structure Interaction (FSI) interface combines the extracellular fluid domain with solid cytoplasm domain to capture the shear stress transmission. The FSI interface uses an arbitrary Lagrangian-Eulerian (ALE) method to combine fluid flow, represented using the Eulerian description and a spatial coordinate system, with solid mechanics, represented using the Lagrangian description and a material coordinate system. The boundary condition of the biochemical species transport was set as the flux condition to mimics the biochemical reaction at the (sub)cellular boundaries, including the basal plane, focal adhesion, nuclear membrane, and cell membrane. The unidirectional laminar flow simulations are performed for 24 or 72 hours in 0.1s timesteps, which grow exponentially to speed up the calculations. Oscillatory flow simulations shortened the process of actin cap formation and nucleus stiffness change over 24

hours, calculated in uniform 0.25s time steps for 8.64s to speed up the calculation.

QUANTIFICATION AND STATISTICAL ANALYSIS

Measurements of Nuclear/Cytoplasmic Ratio of YAP. The YAP ratio (YR) values were measured using image segmentation and quantifying the ratio of YAP intensity inside the nucleus to YAP intensity in cytoplasm. After projecting the maximum intensity of the image series onto a layer in ImageJ 1.5.3q[61], we segmented the cytoplasmic YAP from the background using Cellpose, a pretrained deep learning-based segmentation method[67]. Then, we labeled the cell nucleus stained with DAPI via StarDist convolutional neural network[68,69]. Then, the mean fluorescence intensity of YAP staining in the nucleus and cytoplasm were measured respectively.

Measurements of Chromatin Compaction with Nuclear DAPI Staining. Here, we used the microscopy-based approaches[30] to assess the degree of heterogeneity of DNA signal across the nucleus of ECs exposed to shear stress by quantifing the coefficient of variation of DAPI intensity[70,71]. After segmenting the nucleus with StarDist convolutional neural network[68,69], the coefficient of variation (CV) of individual nucleus is calculated as the ratio of standard deviation of the DAPI intensity values to the mean value of intensity of the nucleus. The segmentation of nucleus with StarDist was achieved in ImageJ 1.5.3q, and the standard deviation and the mean value of the DAPI intensity were calculated in MATLAB R2021a.

Statistical Analysis. Data was analyzed using GraphPad Prism 9.0 software and were presented as mean ± SD. Sample numbers and experimental repeats were described in the figure legends. Statistical significance for samples was determined using two-tailed unpaired Student's *t* test. Data were considered statistically significant if $P < 0.05$.

RESOURCE AVAILABILITY

All data and code supporting the current study are available from the corresponding author upon request.

References

1. Chaudhuri, O., Cooper-White, J., Janmey, P.A., Mooney, D.J., and Shenoy, V.B. (2020). Effects of extracellular matrix viscoelasticity on cellular behaviour. Nature *584*, 535-546.

2. Kim, J.-K., Louhghalam, A., Lee, G., Schafer, B.W., Wirtz, D., and Kim, D.-H. (2017). Nuclear lamin A/C harnesses the perinuclear apical actin cables to protect nuclear morphology. Nature communications *8*, 1-13.

3. Xu, J., Mathur, J., Vessières, E., Hammack, S., Nonomura, K., Favre, J., Grimaud, L., Petrus, M., Francisco, A., and Li, J. (2018). GPR68 senses flow and is essential for vascular physiology. Cell *173*, 762-775. e716.

4. Hahn, C., and Schwartz, M.A. (2009). Mechanotransduction in vascular physiology and atherogenesis. Nature reviews Molecular cell biology *10*, 53-62.

5. Jaalouk, D.E., and Lammerding, J. (2009). Mechanotransduction gone awry. Nature reviews Molecular cell biology *10*, 63-73.

6. Swartz, M.A., and Lund, A.W. (2012). Lymphatic and interstitial flow in the tumour microenvironment: linking mechanobiology with immunity. Nature Reviews Cancer *12*, 210-219.

7. Lee, J.Y., Chang, J.K., Dominguez, A.A., Lee, H.-p., Nam, S., Chang, J., Varma, S., Qi, L.S., West, R.B., and Chaudhuri, O. (2019). YAP-independent mechanotransduction drives breast cancer progression. Nature communications *10*, 1-9.

8. Cooper, J., and Giancotti, F.G. (2019). Integrin signaling in cancer: mechanotransduction, stemness, epithelial plasticity, and therapeutic resistance. Cancer cell *35*, 347-367.

9. Kwak, B.R., Bäck, M., Bochaton-Piallat, M.-L., Caligiuri, G., Daemen, M.J., Davies, P.F., Hoefer, I.E., Holvoet, P., Jo, H., and Krams, R. (2014). Biomechanical factors in atherosclerosis: mechanisms and clinical implications. European heart journal *35*, 3013-3020.

10. Linder, S., Cervero, P., Eddy, R., and Condeelis, J. (2022). Mechanisms and roles of podosomes and invadopodia. Nature Reviews Molecular Cell Biology. 10.1038/s41580-022-00530-6.

11. Wang, L., Luo, J.-Y., Li, B., Tian, X.Y., Chen, L.-J., Huang, Y., Liu, J., Deng, D., Lau, C.W., and Wan, S. (2016). Integrin-YAP/TAZ-JNK cascade mediates atheroprotective effect of unidirectional shear flow. Nature *540*, 579-582.

12. Nakajima, H., Yamamoto, K., Agarwala, S., Terai, K., Fukui, H., Fukuhara, S., Ando, K., Miyazaki, T., Yokota, Y., and Schmelzer, E. (2017). Flow-dependent endothelial YAP regulation contributes to vessel maintenance. Developmental cell *40*, 523-536. e526.

13. Dupont, S., Morsut, L., Aragona, M., Enzo, E., Giulitti, S., Cordenonsi, M., Zanconato, F., Le Digabel, J., Forcato, M., and Bicciato, S. (2011). Role of YAP/TAZ in mechanotransduction. Nature *474*, 179-183.

14. Panciera, T., Azzolin, L., Cordenonsi, M., and Piccolo, S. (2017). Mechanobiology of YAP and TAZ in physiology and disease. Nature reviews Molecular cell biology *18*, 758-770.

15. Zhao, B., Lei, Q.-Y., and Guan, K.-L. (2008). The Hippo–YAP pathway: new connections between regulation of organ size and cancer. Current opinion in cell biology *20*, 638-646.

16. Piccolo, S., Dupont, S., and Cordenonsi, M. (2014). The biology of YAP/TAZ: hippo signaling and beyond. Physiological reviews.

17. Wang, K.-C., Yeh, Y.-T., Nguyen, P., Limqueco, E., Lopez, J., Thorossian, S., Guan, K.-L., Li, Y.-S.J., and Chien, S. (2016). Flow-dependent YAP/TAZ activities regulate endothelial phenotypes and atherosclerosis. Proceedings of the National Academy of Sciences *113*, 11525-11530.

18. Yuan, P., Hu, Q., He, X., Long, Y., Song, X., Wu, F., He, Y., and Zhou, X. (2020). Laminar flow inhibits the Hippo/YAP pathway via autophagy and SIRT1-mediated deacetylation against atherosclerosis. Cell death & disease *11*, 1-11.

19. Xu, S., Koroleva, M., Yin, M., and Jin, Z.G. (2016). Atheroprotective laminar flow inhibits Hippo pathway effector YAP in endothelial cells. Translational Research *176*, 18-28. e12.

20. Elosegui-Artola, A., Andreu, I., Beedle, A.E., Lezamiz, A., Uroz, M., Kosmalska, A.J., Oria, R., Kechagia, J.Z., Rico-Lastres, P., and Le Roux, A.-L. (2017). Force triggers YAP nuclear entry by regulating transport across nuclear pores. Cell *171*, 1397-1410. e1314.

21. Andreu, I., Granero-Moya, I., Chahare, N.R., Clein, K., Molina-Jordán, M., Beedle, A.E., Elosegui-Artola, A., Abenza, J.F., Rossetti, L., and Trepat, X. (2022). Mechanical force application to the nucleus regulates nucleocytoplasmic transport. Nature Cell Biology, 1-10.

22. Khatau, S.B., Hale, C.M., Stewart-Hutchinson, P., Patel, M.S., Stewart, C.L., Searson, P.C., Hodzic, D., and Wirtz, D. (2009). A perinuclear actin cap regulates nuclear shape. Proceedings of the National Academy of Sciences *106*, 19017-19022.

23. Chambliss, A.B., Khatau, S.B., Erdenberger, N., Robinson, D.K., Hodzic, D., Longmore, G.D., and Wirtz, D. (2013). The LINC-anchored actin cap connects the extracellular milieu to the nucleus for ultrafast mechanotransduction. Scientific reports *3*, 1-9.

24. Alisafaei, F., Jokhun, D.S., Shivashankar, G., and Shenoy, V.B. (2019). Regulation of nuclear architecture, mechanics, and nucleocytoplasmic shuttling of epigenetic factors by cell geometric constraints. Proceedings of the National Academy of Sciences *116*, 13200-13209.

25. Wong, A.J., Pollard, T.D., and Herman, I.M. (1983). Actin filament stress fibers in vascular endothelial cells in vivo. Science *219*, 867-869.

26. Flaherty, J.T., Pierce, J.E., Ferrans, V.J., Patel, D.J., TUCKER, W.K., and FRY, D.L. (1972). Endothelial nuclear patterns in the canine arterial tree with particular reference to hemodynamic events. Circulation research *30*,

23-33.

27. Bailey, M., Alunni-Cardinali, M., Correa, N., Caponi, S., Holsgrove, T., Barr, H., Stone, N., Winlove, C.P., Fioretto, D., and Palombo, F. (2020). Viscoelastic properties of biopolymer hydrogels determined by Brillouin spectroscopy: A probe of tissue micromechanics. Science advances *6*, eabc1937.

28. Stephens, A.D., Banigan, E.J., Adam, S.A., Goldman, R.D., and Marko, J.F. (2017). Chromatin and lamin A determine two different mechanical response regimes of the cell nucleus. Molecular biology of the cell *28*, 1984-1996.

29. Nava, M.M., Miroshnikova, Y.A., Biggs, L.C., Whitefield, D.B., Metge, F., Boucas, J., Vihinen, H., Jokitalo, E., Li, X., and Arcos, J.M.G. (2020). Heterochromatin-driven nuclear softening protects the genome against mechanical stress-induced damage. Cell *181*, 800-817. e822.

30. Martin, L., Vicario, C., Castells-García, Á., Lakadamyali, M., Neguembor, M.V., and Cosma, M.P. (2021). A protocol to quantify chromatin compaction with confocal and super-resolution microscopy in cultured cells. STAR protocols *2*, 100865.

31. Kim, D.-H., Khatau, S.B., Feng, Y., Walcott, S., Sun, S.X., Longmore, G.D., and Wirtz, D. (2012). Actin cap associated focal adhesions and their distinct role in cellular mechanosensing. Scientific reports *2*, 1-13.

32. Rangamani, P., Lipshtat, A., Azeloglu, E.U., Calizo, R.C., Hu, M., Ghassemi, S., Hone, J., Scarlata, S., Neves, S.R., and Iyengar, R. (2013). Decoding information in cell shape. Cell *154*, 1356-1369.

33. Scott, K.E., Fraley, S.I., and Rangamani, P. (2021). A spatial model of YAP/TAZ signaling reveals how stiffness, dimensionality, and shape contribute to emergent outcomes. Proceedings of the National Academy of Sciences *118*, e2021571118.

34. Novev, J.K., Heltberg, M.L., Jensen, M.H., and Doostmohammadi, A. (2021). Spatiotemporal model of cellular mechanotransduction via Rho and YAP. Integrative Biology *13*, 197-209.

35. Chachisvilis, M., Zhang, Y.-L., and Frangos, J.A. (2006). G protein-coupled receptors sense fluid shear stress in endothelial cells. Proceedings of the National Academy of Sciences *103*, 15463-15468.

36. Zhou, J., Li, Y.-S., and Chien, S. (2014). Shear stress–initiated signaling and its regulation of endothelial function. Arteriosclerosis, thrombosis, and vascular biology *34*, 2191-2198.

37. Hoare, S.R., Tewson, P.H., Quinn, A.M., Hughes, T.E., and Bridge, L.J. (2020). Analyzing kinetic signaling data for G-protein-coupled receptors. Scientific reports *10*, 1-23.

38. Wan, Q., Kim, S.J., Yokota, H., and Na, S. (2013). Differential activation and inhibition of RhoA by fluid flow induced shear stress in chondrocytes. Cell biology international *37*, 568-576.

39. Shi, Q., Zheng, L., Na, J., Li, X., Yang, Z., Chen, X., Song, Y., Li, C.,

Zhou, L., and Fan, Y. (2022). Fluid shear stress promotes periodontal ligament cells proliferation via p38-Amot-YAP/TAZ. Cellular and Molecular Life Sciences *79*, 1-18.

40. Wintner, O., Hirsch - Attas, N., Schlossberg, M., Brofman, F., Friedman, R., Kupervaser, M., Kitsberg, D., and Buxboim, A. (2020). A unified linear viscoelastic model of the cell nucleus defines the mechanical contributions of lamins and chromatin. Advanced Science *7*, 1901222.

41. Miller, P.W., Fortunato, D., Muratov, C., Greengard, L., and Shvartsman, S. (2022). Forced and spontaneous symmetry breaking in cell polarization. Nature Computational Science *2*, 504-511.

42. De Belly, H., Paluch, E.K., and Chalut, K.J. (2022). Interplay between mechanics and signalling in regulating cell fate. Nature Reviews Molecular Cell Biology, 1-16.

43. Dessalles, C.A., Leclech, C., Castagnino, A., and Barakat, A.I. (2021). Integration of substrate-and flow-derived stresses in endothelial cell mechanobiology. Communications Biology *4*, 1-15.

44. Souilhol, C., Serbanovic-Canic, J., Fragiadaki, M., Chico, T.J., Ridger, V., Roddie, H., and Evans, P.C. (2020). Endothelial responses to shear stress in atherosclerosis: a novel role for developmental genes. Nature Reviews Cardiology *17*, 52-63.

45. Chiu, J.-J., and Chien, S. (2011). Effects of disturbed flow on vascular endothelium: pathophysiological basis and clinical perspectives. Physiological reviews *91*, 327-387.

46. Sabine, A., Bovay, E., Demir, C.S., Kimura, W., Jaquet, M., Agalarov, Y., Zangger, N., Scallan, J.P., Graber, W., and Gulpinar, E. (2015). FOXC2 and fluid shear stress stabilize postnatal lymphatic vasculature. The Journal of clinical investigation *125*, 3861-3877.

47. Lulevich, V., Zimmer, C.C., Hong, H.-s., Jin, L.-w., and Liu, G.-y. (2010). Single-cell mechanics provides a sensitive and quantitative means for probing amyloid-β peptide and neuronal cell interactions. Proceedings of the National Academy of Sciences *107*, 13872-13877.

48. Mitchison, J., and Swann, M. (1954). The mechanical properties of the cell surface. Journal of Experimental Biology *31*, 443-460.

49. Haase, K., Macadangdang, J.K., Edrington, C.H., Cuerrier, C.M., Hadjiantoniou, S., Harden, J.L., Skerjanc, I.S., and Pelling, A.E. (2016). Extracellular forces cause the nucleus to deform in a highly controlled anisotropic manner. Scientific reports *6*, 1-11.

50. Shimamoto, Y., Tamura, S., Masumoto, H., and Maeshima, K. (2017). Nucleosome–nucleosome interactions via histone tails and linker DNA regulate nuclear rigidity. Molecular biology of the cell *28*, 1580-1589.

51. Killaars, A.R., Grim, J.C., Walker, C.J., Hushka, E.A., Brown, T.E., and Anseth, K.S. (2019). Extended exposure to stiff microenvironments leads to persistent chromatin remodeling in human mesenchymal stem cells.

Advanced Science *6*, 1801483.

52. Poli, A., Pennacchio, F.A., Nastaly, P., Ghisleni, A., Crestani, M., Pramotton, F.M., Iannelli, F., Beznusenko, G., Mironov, A.A., and Panzetta, V. (2022). PIP4K2B is a mechanosensor and induces heterochromatin-driven nuclear softening through UHRF1. bioRxiv.

53. Luciano, M., Xue, S.-L., De Vos, W.H., Redondo-Morata, L., Surin, M., Lafont, F., Hannezo, E., and Gabriele, S. (2021). Cell monolayers sense curvature by exploiting active mechanics and nuclear mechanoadaptation. Nature Physics *17*, 1382-1390.

54. Meagher, R.B., Kandasamy, M.K., Deal, R.B., and McKinney, E.C. (2007). Actin-related proteins in chromatin-level control of the cell cycle and developmental transitions. Trends in cell biology *17*, 325-332.

55. Kapoor, P., and Shen, X. (2014). Mechanisms of nuclear actin in chromatin-remodeling complexes. Trends in cell biology *24*, 238-246.

56. Shiu, J.-Y., Aires, L., Lin, Z., and Vogel, V. (2018). Nanopillar force measurements reveal actin-cap-mediated YAP mechanotransduction. Nature cell biology *20*, 262-271.

57. Koushki, N., Ghagre, A., Srivastava, L.K., Sitaras, C., Yoshie, H., Molter, C., and Ehrlicher, A.J. (2020). Lamin A redistribution mediated by nuclear deformation determines dynamic localization of YAP. BioRxiv.

58. Hou, Y., Xie, W., Yu, L., Camacho, L.C., Nie, C., Zhang, M., Haag, R., and Wei, Q. (2020). Surface roughness gradients reveal topography-specific mechanosensitive responses in human mesenchymal stem cells. Small *16*, 1905422.

59. Dong, J.-d., Gu, Y.-q., Li, C.-m., Wang, C.-r., Feng, Z.-g., Qiu, R.-x., Chen, B., Li, J.-x., Zhang, S.-w., and Wang, Z.-g. (2009). Response of mesenchymal stem cells to shear stress in tissue-engineered vascular grafts. Acta pharmacologica sinica *30*, 530-536.

60. Zhong, W., Tian, K., Zheng, X., Li, L., Zhang, W., Wang, S., and Qin, J. (2013). Mesenchymal stem cell and chondrocyte fates in a multishear microdevice are regulated by Yes-associated protein. Stem cells and development *22*, 2083-2093.

61. Schneider, C.A., Rasband, W.S., and Eliceiri, K.W. (2012). NIH Image to ImageJ: 25 years of image analysis. Nature methods *9*, 671-675.

62. Zhao, P., Liu, X., Zhang, X., Wang, L., Su, H., Wang, L., He, N., Zhang, D., Li, Z., and Kang, H. (2021). Flow shear stress controls the initiation of neovascularization via heparan sulfate proteoglycans within a biomimetic microfluidic model. Lab on a Chip *21*, 421-434.

63. Zhang, J., and Scarcelli, G. (2021). Mapping mechanical properties of biological materials via an add-on Brillouin module to confocal microscopes. Nature protocols *16*, 1251-1275.

64. Berghaus, K.V., Yun, S.H., and Scarcelli, G. (2015). High speed sub-GHz spectrometer for Brillouin scattering analysis. JoVE (Journal of

Visualized Experiments), e53468.

65. Edrei, E., Gather, M.C., and Scarcelli, G. (2017). Integration of spectral coronagraphy within VIPA-based spectrometers for high extinction Brillouin imaging. Optics express *25*, 6895-6903.

66. Scarcelli, G., Polacheck, W.J., Nia, H.T., Patel, K., Grodzinsky, A.J., Kamm, R.D., and Yun, S.H. (2015). Noncontact three-dimensional mapping of intracellular hydromechanical properties by Brillouin microscopy. Nature methods *12*, 1132-1134.

67. Stringer, C., Wang, T., Michaelos, M., and Pachitariu, M. (2021). Cellpose: a generalist algorithm for cellular segmentation. Nature methods *18*, 100-106.

68. Schmidt, U., Weigert, M., Broaddus, C., and Myers, G. (2018). Cell Detection with Star-convex Polygons. arXiv preprint arXiv:1806.03535.

69. Weigert, M., Schmidt, U., Haase, R., Sugawara, K., and Myers, G. (2019). Star-convex Polyhedra for 3D Object Detection and Segmentation in Microscopy. arXiv e-prints, arXiv: 1908.03636.

70. Grézy, A., Chevillard-Briet, M., Trouche, D., and Escaffit, F. (2016). Control of genetic stability by a new heterochromatin compaction pathway involving the Tip60 histone acetyltransferase. Molecular biology of the cell *27*, 599-607.

71. Neguembor, M.V., Martin, L., Castells-García, Á., Gómez-García, P.A., Vicario, C., Carnevali, D., Abed, J.A., Granados, A., Sebastian-Perez, R., and Sottile, F. (2021). Transcription-mediated supercoiling regulates genome folding and loop formation. Molecular Cell *81*, 3065-3081. e3012.